Journal of the Mechanics and Physics of Solids 135 (2020) 103781

Contents lists available at ScienceDirect

Journal of the Mechanics and Physics of Solids

journal homepage: www.elsevier.com/locate/jmps

The nonlinear elastic response of filled elastomers: Experiments vs. theory for the basic case of particulate fillers of micrometer size

Marc Leonard [a], Naibin Wang [a], Oscar Lopez-Pamies [b,*], Toshio Nakamura [a]

[a] Department of Mechanical Engineering, Stony Brook University, Stony Brook, NY 11794, USA
[b] Department of Civil and Environmental Engineering, University of Illinois, Urbana–Champaign, IL 61801, USA

ARTICLE INFO

Article history:
Received 4 July 2019
Revised 6 September 2019
Accepted 7 November 2019
Available online 8 November 2019

Keywords:
Elastomers
Fillers
Finite deformation
Homogenization
Reinforcement

ABSTRACT

Standard particulate fillers utilized to enhance the macroscopic elasticity of elastomers — most notably, carbon black and silica particles — are inherently of nanometer size. Because their size is comparable to the typical lengths of the polymer chain segments between crosslinks in the embedding elastomers, there is a plurality of microscopic mechanisms by which such fillers provide macroscopic enhancement. Well-known among these is the so-called *hydrodynamic effect*, which has long been thought to become increasingly dominant as the size of the fillers increases from nanometer to micrometer or larger length scales. This paper reports a combined experimental/theoretical investigation aimed at critically examining such a belief by isolating — that is, by excluding the presence of other enhancing mechanisms, such as interphases and occluded rubber — and quantifying the hydrodynamic effect behind the enhanced nonlinear elastic response of a prototypical class of particle-filled elastomers: polydimethylsiloxane (PDMS) featuring various cross-link densities filled with an isotropic distribution of glass spherical particles of monodisperse micrometer size. The close agreement found between the experiments for a variety of filled PDMS elastomers with the predictions based on recently developed rigorous homogenization results corroborate that the observed enhancement in the nonlinear elastic response of the PDMS elastomers upon the addition of the glass particles is indeed solely due to the hydrodynamic effect. In addition to filling a lacuna in the basic experimental knowledge of filled elastomers, the findings reported here also have direct practical implications on the modeling of a number of emerging active filled elastomers, such as for instance magnetorheological elastomers, wherein the iron filler particles — in contrast to standard fillers — are typically micrometer in size.

1. Introduction

Owing to the multifaceted benefits that they provide, carbon black and silica have long been pervasively used as the preferred fillers to enhance the elasticity and numerous other mechanical properties of elastomers; see, e.g., Wiegand (1937), Wagner (1976), Leblanc (2010). However, because of the inherent nanometer size of carbon black and silica fillers, the mul-

* Corresponding author.
E-mail address: pamies@illinois.edu (O. Lopez-Pamies).

https://doi.org/10.1016/j.jmps.2019.103781
0022-5096/

tiple mechanisms by which they provide enhancement — as is the case with other emerging nanofillers — still remain quantitatively unresolved to date; for recent progress on the subject, see, for instance, the works of Heinrich et al. (2002), Frogley et al. (2003), Berriot et al. (2003), Fukahori (2007), Mark and Erman (2007), Zou et al. (2008), Valentin et al. (2008), Qu et al. (2011), Benevides and Nunes (2015), Tadiello et al. (2015), Song and Zheng (2016) and Meddeb et al. (2019). Omnipresent among the various possible enhancing mechanisms is the so-called *hydrodynamic effect*,[1] which refers to the aprirorism that the addition of fillers to an elastomer results in a two-phase composite material whose macroscopic elastic properties are, by construction, some "weighted" average of the elastic properties of the soft elastomer and the comparatively rigid fillers. It is now well understood that the "weights" in that average depend on the specifics of the amount, the shape, and the spatial distribution of the filler particles and are determined by means of the homogenization of the governing elasticity equations; see, e.g., Hill (1972), Braides (1985), and Müller (1987).

While the hydrodynamic effect is commonly expected to become increasingly dominant as the size of the fillers increases and, more critically, to constitute the sole enhancing mechanism for the case when the fillers are micrometer or larger in size (i.e., when the fillers are much larger than the average length of the underlying polymer chain segments between crosslinks in the elastomer), experimental investigations of such a pivotal expectation do not appear to have been reported in the literature, especially at finite deformations. From a theoretical perspective, by contrast, the recent works of Lopez-Pamies et al. (2013a,b), Goudarzi et al. (2015), and Lefévre and Lopez-Pamies (2017a,b) have provided a fairly general string of rigorous[2] analytical and numerical homogenization results that describe the macroscopic nonlinear elastic response of isotropic incompressible elastomers embedding isotropic distributions of filler particles directly in terms not only of the hydrodynamic effect but also of other well-established enhancing mechanisms. Indeed, the more general version of these results presented in Lefévre and Lopez-Pamies (2017b) applies to filler particles of any content, any shape, and any spatial distribution, as well as accounts for the presence of interphases, often referred to as bound rubber, and of the so-called occluded rubber.

In this context, the first objective of this paper is to report an integrated set of experimental results that are aimed precisely at isolating and quantifying the hydrodynamic effect in the macroscopic elastic response of a prototypical class of synthetic elastomers — namely, polydimethylsiloxane (PDMS) elastomers featuring various cross-link densities — by the addition of prototypical fillers of micrometer size — namely, glass spherical particles of about 50 μm in diameter — over a wide range of quasistatic *homogeneous* and *non-homogeneous* finite deformations; the focus here is on the fundamental case of isotropic additions of a moderate amount of fillers sufficiently away from percolation, in this paper, $c = 10\%$ in volume fraction. The second objective is to analyze such experimental results qualitatively and quantitatively by confronting them directly with the aforementioned corresponding theoretical homogenization results.

The organization of the paper is as follows. Section 2 outlines the fabrication process of the unfilled as well as of the filled PDMS elastomers and presents optical microscopy images of the microstructures of the latter. Section 3 describes the uniaxial tension tests performed on the fabricated specimens and reports the experimental results of their macroscopic stress-stretch responses. Section 4 introduces the constitutive models that are employed to describe the nonlinear elastic response of the various PDMS elastomers featuring different cross-link densities used to make the specimens. Section 5 presents the theoretical analysis of the experiments reported in Section 3. Specifically, the results in Subsection 5.1 correspond to computational finite-element (FE) homogenization solutions, whereas those in Subsection 5.2 correspond to the analytical homogenization solution introduced in Lopez-Pamies et al. (2013b). Section 6 presents additional experimental results and the corresponding theoretical analysis of the stretching of specimens containing a cylindrical hole. Finally, Section 7 places on record a number of conclusions.

2. Specimen fabrication

The fabrication of elastomers filled with particles of micrometer or larger size requires careful steps that differ from those routinely followed for elastomers filled with the more standard particles of nanometer size.

Materials: the elastomers and the filler particles. In this work, the class of elastomers used in all of the fabricated specimens is the popular PDMS Sylgard 184 supplied by Dow Corning as a two-part kit, which comprises a base liquid and a curing agent; we also explored the use of other silicone-based elastomers, such as Bluesil RTV 3040 and 4130, but those exhibited an extremely poor adhesion to the glass filler particles and were therefore discarded. Precision sieve calibration glass beads obtained from Corpuscular Inc. were used for the filler particles. These are essentially spherical in shape and monodisperse in size with diameters narrowly ranging from 53 to 63 μm.

The choice of PDMS Sylgard 184 was motivated by several of its attributes. It is a class of elastomers that: (*i*) exhibits almost purely elastic behavior with very little viscous dissipation, (*ii*) provides facile access to a wide range of cross-link densities, (*iii*) is transparent and thus amenable to optical microscopy through its volume, and (*iv*) can feature fairly strong

[1] This effect is also sometimes referred to as the strain amplification effect, a term coined by Mullins and Tobin (1965). The more pervasive terminology of hydrodynamic effect stems from earlier analogous studies on the macroscopic viscosity of suspensions of particles in viscous fluids (Einstein, 1906; Guth and Gold, 1938; Smallwood, 1944).

[2] Prior to these results, starting with the pioneering work of Mullins and Tobin (1965), a plurality of approximations were proposed in the literature either based on heuristic or on variational arguments; see, e.g., Meinecke and Taftaf (1988), Govindjee and Simo (1991), Bergström and Boyce (1999) and Lopez-Pamies and Ponte Castañeda (2006).

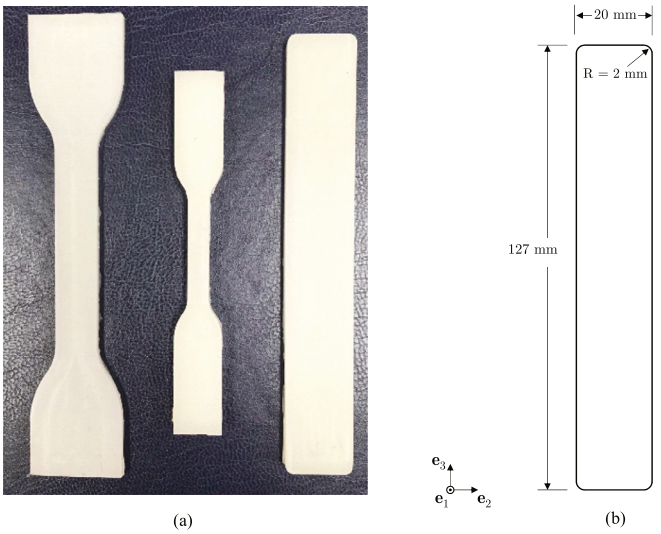

Fig. 1. (a) Photographs of the three different specimen geometries utilized in the uniaxial tension tests for the unfilled and the filled PDMS elastomers. (b) Schematic with dimensions (thickness 3 mm) and laboratory frame of reference for the rectangular specimen.

adhesion to glass. The rationale behind the choice of the glass beads as fillers is that their size and shape are accurately known from the outset and, once embedded, their spatial distribution within the specimens can be readily visualized simply by means of optical microscopy.

Specimens. Fig. 1(a) shows the three types of specimen geometries that were utilized in the experiments to probe the response of the elastomers under uniaxial tension. The discrepancies in the responses measured from different specimen shapes and sizes were checked to be negligibly small; all the results reported in this paper pertain to specimens with the rectangular geometry whose dimensions are indicated in Fig. 1(b). The main issue in obtaining accurate measurements lied on the setup of the gripping conditions so as to avoid slipping during the mechanical tests. This issue is discussed in detail further below.

Fabrication of the unfilled elastomers. With the objective of directly determining their bulk nonlinear elastic response, which is an essential input needed in the bottom-up analysis presented below in Section 5, we first fabricated and tested specimens of unfilled PDMS elastomers featuring the three weight ratios of base to curing agent of interest in this work, namely, 10:1, 15:1, and 20:1. Larger ratios correspond to smaller cross-link densities and hence softer behaviors and larger extensibilities. The fabrication process of the unfilled specimens can be summarized as follows.

An appropriate weight of base liquid is measured and poured into a container. Then the target amount of curing agent — again, with a base-to-curing-agent weight ratio of 10:1, 15:1, or 20:1 — is measured and subsequently added to and mixed with the base for several minutes. The container with the mixture is placed in a vacuum chamber for about 30 min to degas entrapped air bubbles. Subsequently, the mixture is poured into several molds and these placed again in the vacuum chamber to be degassed once more for about 30 min. After this second degassing, the molds filled with the mixture are placed in an oven (a Benchmaster BTRS environmental chamber) for 6 h at 65 °C, after which the specimens are removed from the molds and — to ensure their fully cured state, c.f. Johnston et al. (2014) — are left at room temperature for at least three days before testing.

Fabrication of the filled elastomers. All the specimens of the filled PDMS elastomers were fabricated with the same volume fraction of particles, namely, $c = 10\%$. The rationale behind this value is that it is large enough to lead to a significant enhancement of the mechanical behaviors of all three types of unfilled PDMS elastomers considered in this work. At the same time, it is small enough to allow without difficulty for the uniform non-percolative dispersion of the particles within the elastomers. The fabrication process of the filled specimens requires additional steps, as described next.

In order to improve their adhesion to the PDMS elastomers, the glass particles were cleaned first with alcohol, then with acetone, and finally they were coated with a thin layer of Dow Corning 92-023 primer; removing the final step of coating the particles with the primer did not have any noticeable impact in obtaining good adhesion between the PDMS elastomers and the glass beads. Right after the base and curing agent have been combined at a specified ratio, the appropriate weight (so that $c = 10\%$) of glass particles is added to the container and subsequently mixed for a few minutes. To avoid the sedimentation of the particles — note that the mass density of the PDMS in liquid form is $1.03\,\mathrm{g/cm^3}$, while that of the glass particles is $2.52\,\mathrm{g/cm^3}$ — and to achieve their uniform dispersion throughout the specimens, the container is then placed in the oven at 65 °C for about 5 min, removed for further mixing, then placed in the oven for about 5 min again. This process is repeated several times (typically three) until the mixture possesses enough viscosity to prevent the sedimentation of the particles. Once the desired viscosity is achieved, the container with the mixture is degassed and then the mixture is poured

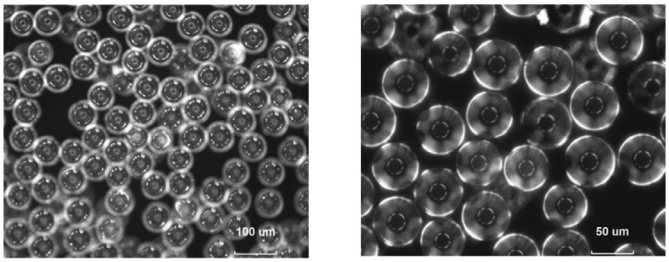

Fig. 2. Optical microscopy images of a filled PDMS specimen at two different magnifications.

Table 1
Specifications of the tested specimens.

Specimens	Base-to-curing-agent weight ratio	Filler ($c = 10\%$)	Initial Young's modulus E_N (MPa)
10N	10:1	No	1.90
15N	15:1	No	0.86
20N	20:1	No	0.65
			E_F (MPa)
10F	10:1	Yes	2.40
15F	15:1	Yes	1.10
20F	20:1	Yes	0.84

into molds and degassed again before placing them back in the oven for the final curing, also carried out at 65 °C for 6 h. We emphasize that the about-outlined process requires a careful monitoring of the viscosity of the mixture, given that if the mixture is overcured, it no longer flows into the molds nor can be degassed.

Fig. 2 shows two representative optical microscopy images of the microstructure of a filled specimen at two different magnifications. These illustrate that the spatial distribution of the particles is uniform, random, and essentially isotropic, as desired; note that the volume fraction of particles appears to be greater than $c = 10\%$ since the micrographs show particles positioned through the thickness. With the naked eye, the filled specimens appear white as shown in Fig. 1(a), however, under the optical microscope, the transparency of the PDMS and the glass beads become apparent.

For subsequent convenience, Table 1 lists and labels the six different types of specimens that were fabricated and tested. At least three separate specimens were made and tested for each type.

3. Uniaxial tension tests

The mechanical behavior of the above-described specimens was probed under states of homogenous deformations via uniaxial tension tests. For definiteness, use was made of the laboratory frame of reference indicated in Fig. 1. Granted the experimentally verified (nearly full) isotropy and incompressibility of the fabricated unfilled and filled elastomers, the first Piola-Kirchhoff stress tensor $\mathbf{S}$ and the deformation gradient tensor $\mathbf{F}$ take then the form $\mathbf{S} = S\mathbf{e}_3 \otimes \mathbf{e}_3$ and $\mathbf{F} = \lambda^{-1/2}(\mathbf{e}_1 \otimes \mathbf{e}_1 + \mathbf{e}_2 \otimes \mathbf{e}_2) + \lambda \mathbf{e}_3 \otimes \mathbf{e}_3$, where λ stands for the applied stretch.

The tests were carried out in a MTS C43 testing system equipped with a 100 N load cell. This load cell was suitably selected in order to monitor accurately the forces involved; the maximum forces reached in each test were in the range of 10 to 40 N. While the forces were measured straightforwardly and accurately, as is typically the case with soft solids, the biggest challenge turned out to be the accurate measuring of the deformations. Two methods were employed. One set of measurements was obtained from the cross-head displacement recorded by the MTS C43 testing machine itself. The other set of measurements was obtained optically via a digital image correlation (DIC) system. Although the employed DIC system can produce both full displacement and full strain fields over the surfaces of the deformed specimens, the latter are not sufficiently accurate when dealing with large deformations. Accordingly, only the displacement measurement capability of the DIC system was utilized in our analysis. Specifically, prior to their testing, the specimens were sprayed with a speckle pattern in order to better resolve the displacement field. During their testing, images were recorded at a frequency of 100 Hz using a Tokina f2.8 AT-X M100 Pro-D Macro lens and the software FlyCapture. The images were analyzed with the software VIC-2D in order to extract the full displacement field. We remark here that we did not use the DIC system for all the tests, since its use requires taking and storing hundreds of photographs for a single load cycle. Given that we fabricated 50+ specimens and each was tested between 3 and 5 cycles of loading/unloading, data acquisition and interpretation with DIC for all of them was not viable. Instead, we relied on the displacement measurements obtained from the MTS C43 testing machine, which were checked to be consistent with those obtained from the DIC system.

Given that our main goal is to investigate the hydrodynamic effect provided by the addition of the glass filler particles over the entire range of possible (small and large) deformations, the specimens were elongated up to stretches near or all

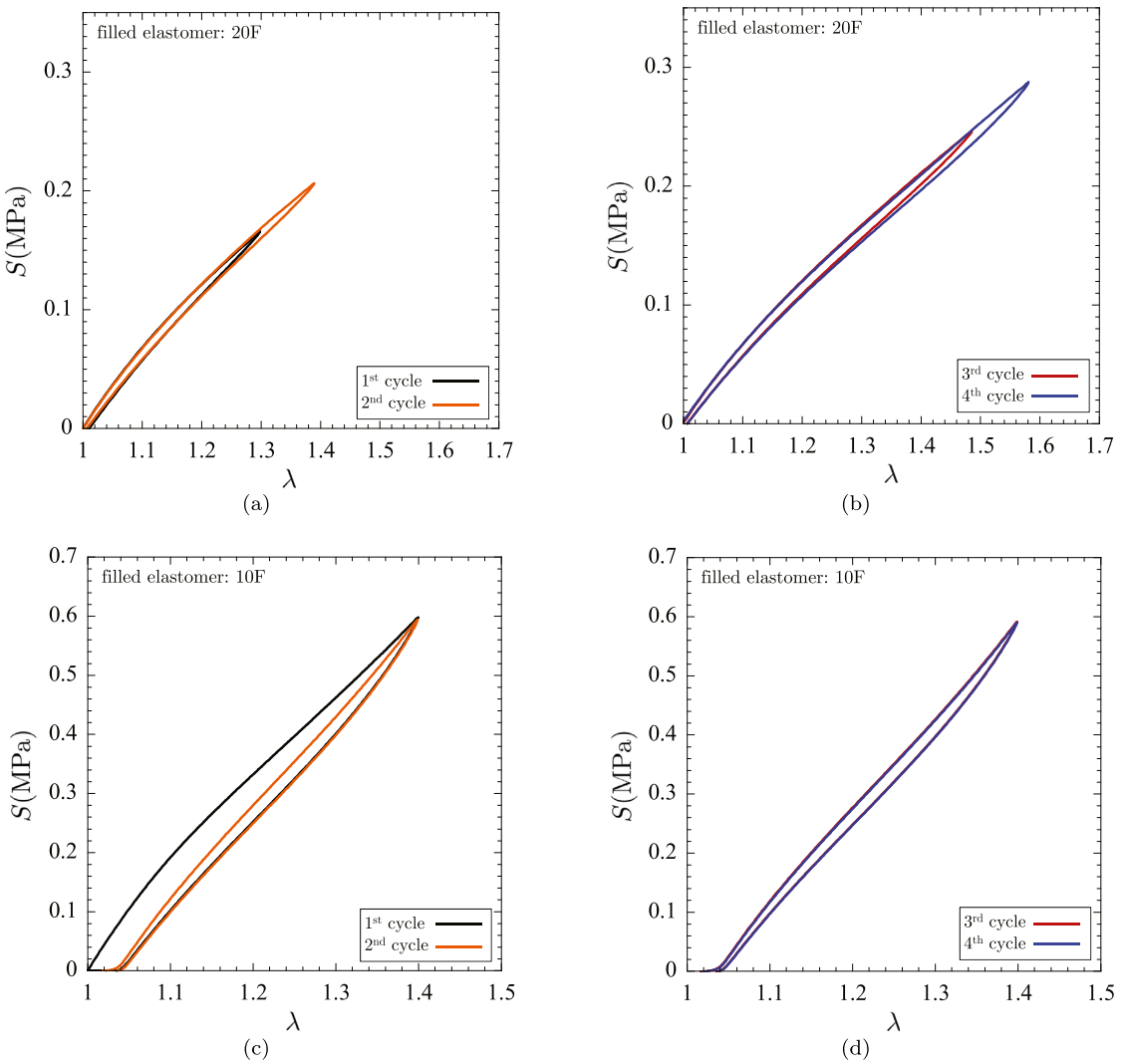

Fig. 3. Representative uniaxial tension responses of the filled PDMS elastomers over four cycles of loading/unloading. The results are shown for the nominal stress S as a function of the applied stretch λ. Parts (a)–(b) show cycles 1–2 and 3–4 for a filled PDMS elastomer with a ratio 20:1 of base to curing agent (20F) under cyclicly increased maximum stretch ($\lambda_{max} = 1.3, 1.4, 1.5, 1.6$). Parts (c)–(d) show cycles 1–2 and 3–4 for a filled PDMS elastomer with 10:1 ratio of base to curing agent (10F) under cyclicly fixed maximum stretch ($\lambda_{max} = 1.4$).

the way to their failure (which occurred by fracture apparently originating from surface defects near the grips), precisely, up to uniaxial stretches in the range of $\lambda = 1.30$ to 1.70. Now, because of their incompressibility, the specimens become thinner as the applied stretch is increased. This leads to the loosening of the grips and in turn to the possible slipping of the specimens. Since conventional gripping fixtures are not suitable to hold soft specimens, we acquired a set of screw action grips with self-pivoting faces. These grips lowered the amount of slipping compared to the conventional grips, but still they did not maintain sufficiently large clamping forces at the larger stretches. Ultimately, we made use of a further modification to the grips, essentially by making use of binder clips to hold the specimens in place. With this configuration, the slipping was negligible for all tests except for those performed on the specimens made with the stiffer PDMS elastomer, that is, the one with 10:1 ratio of base to curing agent. For these stiffer specimens, the stretches measured from the MTS testing machine were suitably calibrated based on comparisons with the stretches measured from the DIC system.

In all, more than 50 uniaxial tension tests were carried out. All of them comprised from 3 to 5 cycles of loading and unloading. The maximum stretch λ_{max} in each cycle was either set constant or monotonically increased. In each test, the loading/unloading time was set at 40 s per complete loading/unloading cycle, which corresponds to stretch rates of around $|\dot{\lambda}| = 0.025\ s^{-1}$. We also carried out tests at 20 and 120 s per cycle and found the results to be nearly identical. This independence of the loading rate is consistent with the findings of Poulain et al. (2018), who reported that PDMS Sylgard 184 elastomers with a broad spectrum of cross-link densities exhibit small viscous dissipation.

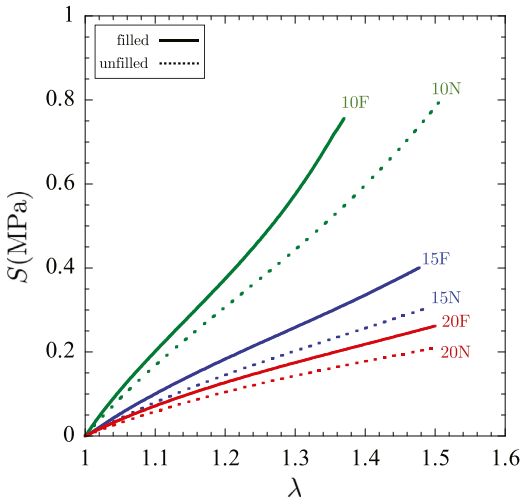

Fig. 4. Experimental measurements of the uniaxial stress-stretch response of the filled (solid lines) and unfilled (dotted lines) PDMS elastomers with the three different ratios of base to curing agent 10:1, 15:1, and 20:1.

Fig. 3 shows typical measurements of the uniaxial stress-stretch response[3] of the filled elastomers. Specifically, Figs. 3(a)–(b) show results for a 20F specimen (i.e., a filled PDMS elastomer with a ratio 20:1 of base to curing agent) for a case when the maximum stretch in each loading/unloading cycle is progressively increased from $\lambda_{max} = 1.3$ to 1.4, 1.5, and finally to 1.6. On the other hand, Figs. 3(c)–(d) show results for a stiffer 10F specimen (i.e., a filled PDMS elastomer with a base to curing agent ratio 10:1) for a case when the maximum stretch is kept constant at $\lambda_{max} = 1.4$ over four loading/unloading cycles. The mechanical behaviors of both types of specimens are not only nonlinear but also exhibit some hysteresis (i.e., different paths for loading and unloading). The 20F specimen exhibits similar behavior for all loading/unloading cycles. This was the case for all specimens (filled and unfilled) 20F, 20N, 15F, and 15N. By contrast, the behavior of the 10F specimen during the first loading is clearly different from that of the subsequent loadings. Moreover, the specimen appears to retain some residual stretch (about $\lambda = 1.02$) upon the first unloading. This was also the behavior observed for all specimens (filled and unfilled) 10F and 10N, for which the residual stretches varied form $\lambda = 1.005$ to 1.04, depending on the specimen type and the maximum applied stretch λ_{max}. In the sequel, we restrict our investigation to the repeatable loading response of the specimens after their first loading/unloading cycle, and do not concern ourselves with their slightly hysteretic behavior thereafter.

Fig. 4 shows the uniaxial stress-stretch response of the filled elastomers 10F, 15F, 20F and the corresponding unfilled elastomers 10N, 15N, 20N. Each plot corresponds to the average response of three different specimens. The maximum difference in the response between any two specimens made of the same material was less than 6% in the nominal stress value S for a given stretch λ; error bars indicating this variation among specimens are not included in Fig. 4 for clarity, but they are included below in subsequent figures where the data for unfilled and filled elastomers is presented separately. The bulk of this variation appears to arise from slight unavoidable differences in the fabrication of the specimens and not from the measurements of the forces and deformations. Indeed, the mechanical behavior of PDMS Sylgard 184 is highly sensitive to its curing so that small differences in the ratio of base to curing agent used in their fabrication, together with differences in the curing time (even after days of curing) can result in small but noticeably different behaviors.

The stress-stretch results in Fig. 4 clearly reveal that the addition of the glass filler particles to all three types of PDMS elastomers leads to a significant enhancement of their elastic response at small as well as at large deformations. The initial tangent moduli of all six results, that is, the initial Young's moduli — labeled, for clarity, E_N for the unfilled elastomers and E_F for the filled — are listed in Table 1. For all three types of PDMS elastomers, the moduli are seen to feature roughly the same increase of about 28% with the addition of fillers. At larger deformations, the enhancement appears to be systematically more pronounced (that is, there is a larger difference between corresponding stress 'F' and 'N' values at any given stretch) in the elastomers with smaller ratio of base to curing agent, that is, in the stiffer and less extensible elastomers. The precise microscopic origin of this enhancement is analyzed in Section 5.

[3] We remark again that the loading/unloading results presented in Fig. 3 correspond to measurements carried out at a constant stretch rate and that the loading starts at $\lambda = 1$ and the unloading finishes also at $\lambda = 1$. This implies that the specimens experience some small amount of compression upon completion of the unloading when returning to $\lambda = 1$.

Table 2
Material constants in the hyperelastic models (1) for the three types of unfilled PDMS elastomers 10N, 15N, 20N. The associated initial Young's moduli E_N are also included for expediency.

Mooney-Rivlin	C_1 (MPa)	C_2 (MPa)	$E_N = 6(C_1 + C_2)$		
10N	0.5107	−0.2412	1.6170		
15N	0.1509	−0.0088	0.8526		
20N	0.0776	0.0313	0.6534		
Ogden	ν_1 (MPa)	ν_2 (MPa)	β_1	β_2	$E_N = 3(\nu_1 + \nu_2)$
10N	0.5053	0.1416	−3.271	6.875	1.9407
15N	0.2851	0.0120	0.875	8.356	0.8913
20N	0.1139	0.1097	2.661	−3.221	0.6708
Lopez-Pamies	μ_1 (MPa)	μ_2 (MPa)	α_1	α_2	$E_N = 3(\mu_1 + \mu_2)$
10N	0.5254	0.0952	2.924	−19.77	1.8618
15N	0.2624	0.0314	1.600	−12.40	0.8814
20N	0.2036	0.0143	0.8393	−34.60	0.6537

4. Hyperelastic models for the unfilled PDMS elastomers

In preparation for the theoretical analysis of the experimental results compiled in Fig. 4, we spell out next the models employed to describe the nonlinear elastic response of each of the unfilled PDMS elastomers 10N, 15N, 20N. Irrespectively of their ratio of base to curing agent, all these three types of elastomers are essentially isotropic and incompressible. For definiteness, we make use of the following well-established isotropic and incompressible hyperelastic stored-energy functions, due to Mooney (1940), Ogden[4] 1972, and Lopez-Pamies (2010a), to model their nonlinear elastic behaviors:

$$W(\mathbf{F}) = \begin{cases} \phi_{\rm MR}(I_1, I_2) = C_1[I_1 - 3] + C_2[I_2 - 3] \\ \varphi_{\rm OG}(\lambda_1, \lambda_2, \lambda_3) = \sum_{r=1}^{2} \dfrac{2}{\beta_r^2} \nu_r \left[\lambda_1^{\beta_r} + \lambda_2^{\beta_r} + \lambda_3^{\beta_r} - 3\right] \\ \psi_{\rm LP}(I_1) = \sum_{r=1}^{2} \dfrac{3^{1-\alpha_r}}{2\alpha_r} \mu_r \left[I_1^{\alpha_r} - 3^{\alpha_r}\right] \end{cases} \tag{1}$$

subject to the incompressibility constraint $\det \mathbf{F} = 1$. In these expressions, $I_1 = \mathbf{F} \cdot \mathbf{F} = \lambda_1^2 + \lambda_2^2 + \lambda_3^2$ and $I_2 = \mathbf{F}^{-T} \cdot \mathbf{F}^{-T} = \lambda_1^2\lambda_2^2 + \lambda_1^2\lambda_3^2 + \lambda_2^2\lambda_3^2$ stand for the first and second principal invariants of the right Cauchy-Green deformation tensor $\mathbf{C} = \mathbf{F}^T\mathbf{F}$, while λ_1, λ_2, λ_3 denote the singular values of the deformation gradient tensor $\mathbf{F}$, i.e., the principal stretches. Note that the required number of material constants are two for the Mooney-Rivlin model, C_1 and C_2, and four for the Ogden and Lopez-Pamies models, ν_1, ν_2, β_1, β_2 and μ_1, μ_2, α_1, α_2, respectively. Considering the three different models (1) shall prove helpful below in the analysis of the experimental results.

For the case of uniaxial tension when $\mathbf{S} = S\mathbf{e}_3 \otimes \mathbf{e}_3$ and $\mathbf{F} = \lambda^{-1/2}(\mathbf{e}_1 \otimes \mathbf{e}_1 + \mathbf{e}_2 \otimes \mathbf{e}_2) + \lambda \mathbf{e}_3 \otimes \mathbf{e}_3$, the nominal stress-stretch relations implied by the stored-energy functions (1) are simply given by

$$S = \frac{dW}{d\lambda}(\mathbf{F}) = \begin{cases} \dfrac{d\phi_{\rm MR}}{d\lambda} = 2C_1\left[\lambda - \lambda^{-2}\right] + 2C_2\left[1 - \lambda^{-3}\right] \\ \dfrac{d\varphi_{\rm OG}}{d\lambda} = \sum_{r=1}^{2} \dfrac{2}{\beta_r} \nu_r \left[\lambda^{\beta_r - 1} - \lambda^{-1-\beta_r/2}\right] \\ \dfrac{d\psi_{\rm LP}}{d\lambda} = \left(\lambda - \lambda^{-2}\right) \sum_{r=1}^{2} 3^{1-\alpha_r} \mu_r \left[\lambda^2 + 2\lambda^{-1}\right]^{\alpha_r - 1} \end{cases} . \tag{2}$$

Relations (2) can be readily fitted via least-squares to the uniaxial tension data in Fig. 4 for the unfilled PDMS elastomers 10N, 15N, 20N. This fitting process (without biasing any subset of data points) renders the values for the material constants listed in Table 2.

The resulting uniaxial stress-stretch relations (2) based on the material constants in Table 2 are plotted in Fig. 5 for direct comparison with the experimental data. In the context of small deformations, the initial Young's moduli described by the three models — given, respectively, by the formulas $E_N = 6(C_1 + C_2)$, $E_N = 3(\nu_1 + \nu_2)$, $E_N = 3(\mu_1 + \mu_2)$ for the Mooney-Rivlin, Ogden, and Lopez-Pamies models — are all in fairly good agreement with the experimental data reported in Table 1. For the PDMS elastomers 15N and 20N with the larger base-to-curing-agent ratios of 15:1 and 20:1, all the hyperelastic models are seen to fit very well the experimental data over the entire range of finite stretches considered. However, for the PDMS elastomer 10N with ratio 10:1, the Ogden and Lopez-Pamies models still show good agreement but the Mooney-Rivlin

[4] Note that we are making use of a notation that is slightly different from the usual one for the material parameter β_r in the Ogden model $(1)_2$.

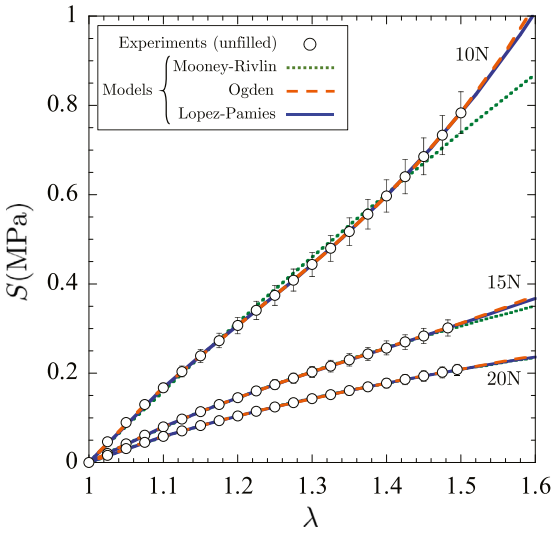

Fig. 5. Comparisons of the measured uniaxial stress-stretch response of the unfilled PDMS elastomers 10N, 15N, 20N (empty circles) and the corresponding predictions (lines) by the hyperelastic models (1), given by formulas (2) with the material constants listed in Table 2.

model exhibits some deviation from the data. This is because the 10N elastomer starts to exhibit limiting chain extensibility already at around a finite stretch of $\lambda = 1.3$, a feature that the Mooney-Rivlin model is known not to account for.

5. Theoretical analysis of the uniaxial tension tests

In this section, we set out to establish that the enhancement exhibited by the filled PDMS elastomers 10F, 15F, 20F in Fig. 4 is entirely due to the hydrodynamic effect.

Microscopic description of the filled PDMS elastomers. To this end, in view of the fabrication process and microscopy results outlined in Section 2 and the uniaxial tension experiments presented in Section 3, we begin by regarding the filled PDMS elastomers as two-phase composite materials made up of a homogeneous isotropic incompressible hyperelastic matrix embedding an isotropic distribution of perfectly bonded[5] rigid[6] particles of the same size and spherical shape. That is, the presence of stiff interphases, or bound rubber, as well as the presence of occluded rubber is ruled out; see, e.g., the works of Goudarzi et al. (2015) and Meddeb et al. (2019) for a discussion on the notable and even dominant enhancement provided by these other mechanisms in elastomers filled with particles of submicron size.

Moreover, we consider that the PDMS elastomer in a given filled specimen exhibits the *same* nonlinear elastic response as the same type of PDMS elastomer would when synthesized in the absence of filler particles. We emphasize that this is *not* expected to be the case in elastomers filled with submicron particles, wherein the matrix material generally exhibits a different (typically softer) response than the same material would when synthesized in the absence of those fillers; see, e.g., Valentin et al. (2008) and Meddeb et al. (2019).

The macroscopic response. Granted the statistically uniform distribution of the glass filler particles and their much smaller size ($\sim 50\,\mu$m) with respect to the smallest size of the specimens (3 mm in thickness), the filled PDMS elastomers can be safely considered as "homogeneous" materials at the length scale of the specimens. Consequently, their macroscopic nonlinear elastic behavior can be determined from their microscopic behavior — that is, from the nonlinear elastic behavior of the underlying PDMS matrix, the rigid behavior of the glass particles, as well as from the amount, shape, and spatial distribution of the particles — through homogenization.

In the next two subsections, we work out two homogenization results by means of two different techniques. Specifically, in Subsection 5.1, we work out the homogenized response of the filled PDMS elastomers computationally, while in Subsection 5.2 we work out their homogenized response analytically by appropriately specializing the results introduced in Lopez-Pamies et al. (2013b).

5.1. Computational homogenization

Following by now a well-established practice (Gusev, 1997; Lefévre and Lopez-Pamies, 2017b; Lopez-Pamies et al., 2013b; Michel et al., 1999; Segurado and Llorca, 2002), the filled elastomers studied in this work can be accurately yet efficiently

[5] The possibility of particle debonding is discussed in Section 7.

[6] For all practical purposes, given that the initial shear modulus of glass is about 70 GPa whereas that of the stiffest PDMS elastomer used in the experiments is in the order of 1 MPa, the glass filler particles can be considered as mechanically rigid.

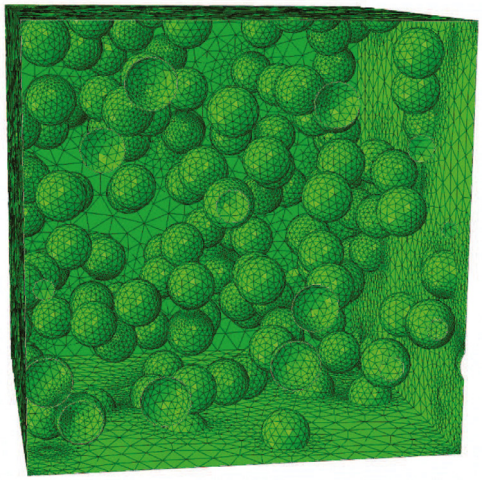

Fig. 6. FE mesh in the undeformed configuration of a representative unit cell $Y_0 = (0, L)^3$ containing a random distribution of $N = 120$ rigid spherical particles at $c = 10\%$ volume fraction.

approximated as infinite media made out of the periodic repetition of a unit cell containing a random distribution of a sufficiently large but finite number N of spherical particles. In the present context, for definiteness, we select the defining unit cell to be a unit cube $Y_0 = (0, L)^3$ with edges of length L that contains a total of $N = 120$ spherical particles of radius $R = L(3c/4\pi N)^{1/3} = 0.05838L$, so that their volume fraction in the unit cell, and hence in the entire composite material, is $c = 10\%$ as in the actual specimens. The interested reader is referred to Section 5.1 in Lopez-Pamies et al. (2013b) and Section 4.2 in Lefévre and Lopez-Pamies (2017b) for details of the construction of realizations with such microstructures via a random sequential adsorption algorithm incorporating geometric constraints that allow for the eventual FE discretization of the resulting unit cells. We emphasize that the number $N = 120$ of particles in the unit cells was carefully selected based on a parametric study that confirmed that it is sufficiently large to render overall nonlinear elastic behaviors for the materials of interest here that are indeed approximately isotropic; the isotropy of the generated microstructures is discussed in further detail in Remark 1.

Having identified the relevant unit cells, the next step is to carry out their spatial discretization. We do so with 10-node tetrahedral quadratic elements by means of the mesh generator code Netgen (Schöbel, 1997). Since the particles are rigid, we do not need to discretize them, instead we constrain the nodes defining their surfaces to undergo the appropriate translations and rotations dictated by the governing equations of elastostatics (Chi et al., 2016) Because of the incompressibility of the matrix material, we employ a hybrid FE formulation in which the elements feature approximations that are quadratic in the displacement field and linear in the pressure field. In particular, since use is made of the commercial FE code ABAQUS to carry out the calculations, we employ the C3D10H hybrid elements built in this code (see ABAQUS Version 6.14 Documentation (2014)). Discretizations with approximately 600,000 elements and 900,000 nodes were checked to produce sufficiently accurate results in the sense that the computed total energy and the average stress over the unit cell exhibited converged values. Fig. 6 shows an example of such a discretization.

The loading is prescribed by enforcing periodic boundary conditions and by increasing the applied average stretch λ in a chosen direction $\mathbf{N}$ with increments smaller than $\Delta\lambda = 0.01$. We remark that the applied average stretch λ in the simulations corresponds precisely to the macroscopic stretch λ applied in the experiments, thus the use of the same symbol. The corresponding nominal stress S is determined by first averaging the computed first Piola-Kirchhoff stress $\mathbf{S}$ over Y_0 and then computing the magnitude $S = \|\mathbf{SN}\|$ of the associated traction in the direction of the applied average stretch; see, e.g., Section 5 and Appendix in Lefévre and Lopez-Pamies (2017b) for further relevant details. In all the simulations, the maximum average stretch was set at $\lambda_{\max} = 1.50$, but many simulations were terminated earlier due to lack of convergence. The primary reason for non-convergence was the excessive distortion of elements between adjacent particles because of the large local stretches that can arise there. This point is illustrated by the contour plots displayed in Fig. 7. These show the maximum $\lambda^{loc}_{\max}$ and minimum $\lambda^{loc}_{\min}$ local stretches as well as the hydrostatic part $\sigma_h = \mathrm{tr}\boldsymbol{\sigma}/3$ of the Cauchy stress $\boldsymbol{\sigma} = \mathbf{SF}^T$ at each material point $\mathbf{x}$ in the deformed configuration of the unit cell Y for a representative case of a 15F specimen at the applied average stretch $\lambda = 1.5$. Note that the local stretch reaches values as large as $\lambda^{loc}_{\max} = 3.1$ in tension and as small as $\lambda^{loc}_{\min} = 0.1$ in compression between adjacent glass particles. The hydrostatic stress σ_h between adjacent glass particles is also clearly seen to exhibit large variations.

Remark 1. *Isotropy of the computational models.* Because of the use of the finite number $N = 120$ of particles in the unit cells, the resulting computational models can only be approximately (and *not* exactly) isotropic. In order to identify the realizations that "best" represent isotropic microstructures out of the tens that we constructed, a series of filtering checks

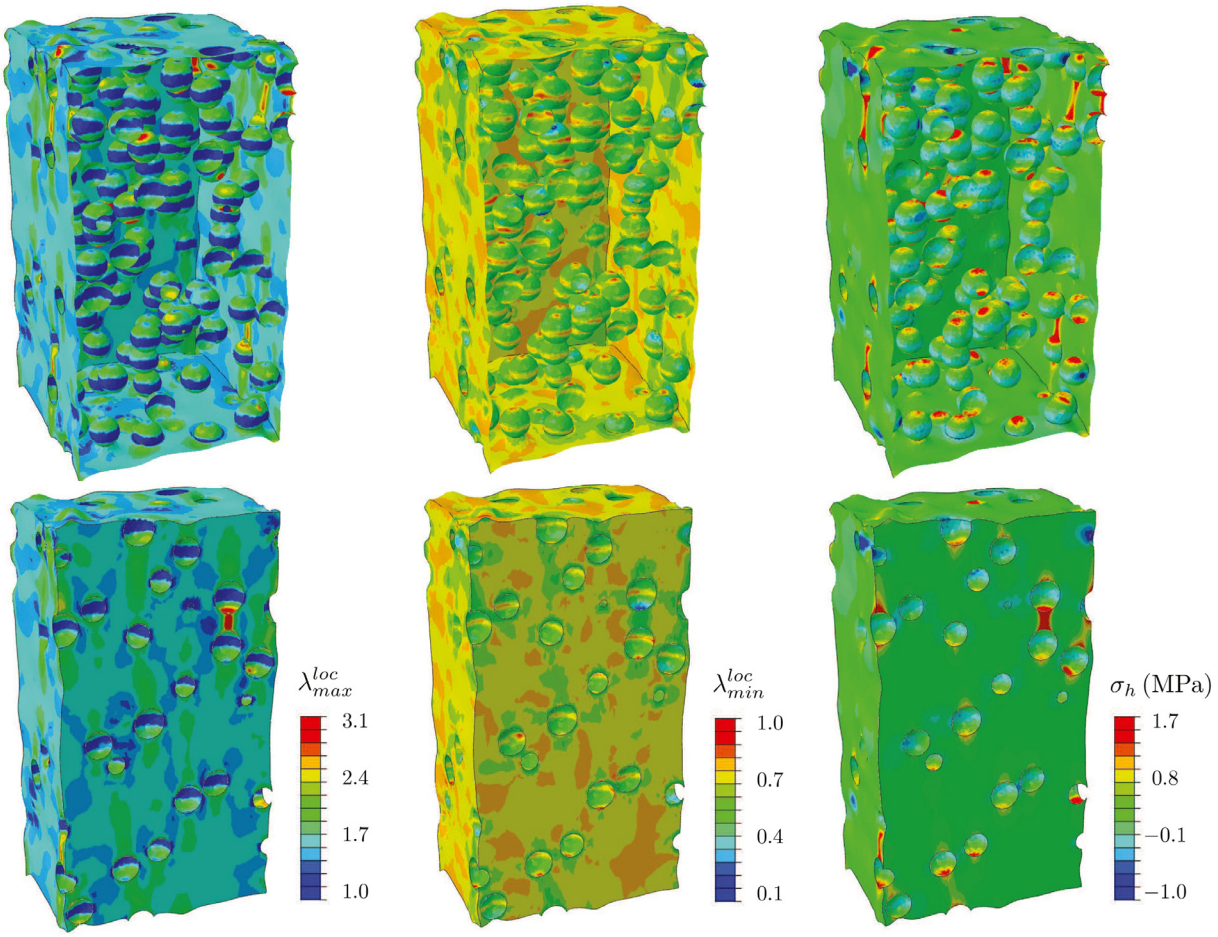

Fig. 7. Contour plots over the deformed configuration of the unit cell Y of the maximum $\lambda^{loc}_{\max}$ and minimum $\lambda^{loc}_{\min}$ local stretches and the hydrostatic part σ_h of the Cauchy stress at the applied average stretch $\lambda = 1.5$ for a 15F specimen wherein the matrix is characterized with the Lopez-Pamies model $(1)_3$ and the material constants given in Table 2. For clarity, the contour plots in the top row show the surfaces of the particles and unit cell boundaries, while those in the bottom row show a representative cross section of the matrix within the unit cell.

on their constitutive response was conducted. First, we checked that their linear elastic response in the small deformation limit is sufficiently isotropic by computing the deviation of their entire homogenized modulus of elasticity tensor from exact isotropy; see Appendix A in Spinelli et al. (2015) for an outline of the involved calculations. Second, we checked that their average uniaxial stress-stretch responses when stretched in several different directions are not substantially different from one another. Realizations were accepted as sufficiently isotropic when such a difference was less than 0.1% under small deformations and gradually increased under larger deformation but remained less than 0.5% at the maximum applied average stretch $\lambda_{\max} = 1.50$. Third, we checked that the co-axiallity between the average Cauchy stress tensor and the average left Green-Cauchy strain tensor over the deformed configuration Y under various types of loading conditions (not just uniaxial tension) remained small. Realizations were accepted as sufficiently isotropic when such a difference was less than 0.05 radians.

We close this remark by noting that due to the weaker nonlinearities of the underlying PDMS elastomers 15N and 20N, the simulations for the specimens 15F and 20F start exhibiting high degrees of isotropy already for unit cells containing just $N = 30$ particles. Because of the stronger nonlinearity of the PDMS elastomer 10N, this is not the case for the simulations for the specimens 10F, thus the need to consider at least $N = 120$. Not all realizations that we generated with $N = 120$ particles turned out to be sufficiently isotropic in the above-outlined sense for the specimens 10F. The FE results that we report in the sequel correspond to the realization that exhibited the highest degree of isotropy.

Fig. 8 shows the macroscopic uniaxial stress-stretch response of the filled PDMS elastomers determined from the FE computations up to the point at which convergence was achieved; note, in particular, that convergence beyond the small stretch of $\lambda = 1.04$ was not achieved for the case of the Mooney-Rivlin 10F model. Results for the cases when the underlying PDMS

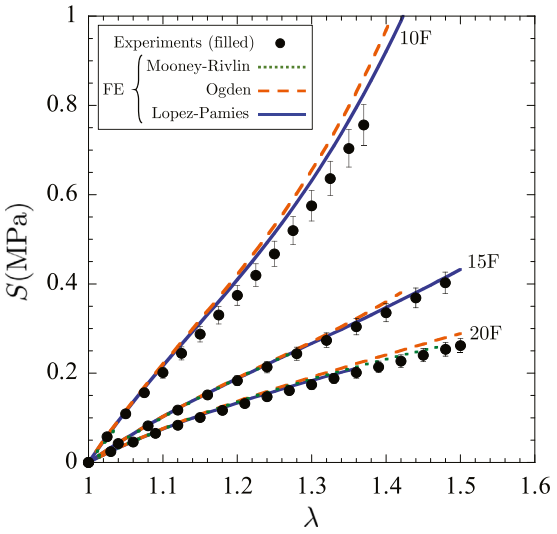

Fig. 8. Comparisons of the FE homogenization predictions (lines) with the experimental data (solid circles) for the uniaxial stress-stretch response of the filled PDMS elastomers 10F, 15F, and 20F. The FE results are shown for all three types of hyperelastic models (1), with the material constants given in Table 2, for the underlying PDMS elastomers.

Table 3
Comparisons of the FE homogenization predictions with the experimental data for the initial Young's modulus E_F of the filled PDMS elastomers 10F, 15F, and 20F.

	E_F (MPa)			
specimens	experiments	FE – Mooney-Rivlin	FE – Ogden	FE – Lopez-Pamies
10F	2.40	2.11	2.53	2.42
15F	1.10	1.11	1.16	1.15
20F	0.84	0.85	0.87	0.85

elastomers are modeled with the Mooney-Rivlin, Ogden, and Lopez-Pamies stored-energy functions (1) and the material constants in Table 2 are all included in the figure. Fig. 8 also includes the experimental results for direct comparison.

A number of observations can be readily made. The primary one is that all three sets of FE results are seen to be in fairly good qualitative and quantitative agreement with the experiments over the entire range of applied stretches. This overall agreement suggests that the enhancement exhibited by the filled PDMS elastomers 10F, 15F, 20F is indeed entirely due to the hydrodynamic effect, as we set out to establish.

There are, however, a few nuances worth recoding. In the context of small deformations, Table 3 shows that the differences between the initial Young's moduli E_F determined from the FE computations and those measured experimentally are by and large within a few percent. For finite deformations, it is also of note that all of the FE predictions consistently feature a slightly stiffer stress-stretch response than the corresponding experimental data. Among the three sets of FE results, the ones wherein the underlying PDMS elastomers are described with the Lopez-Pamies model $(1)_3$ exhibit a closer agreement with the experiments. This despite the fact that the uniaxial stress-stretch response of the Ogden and Lopez-Pamies models are nearly identical for all three unfilled PDMS elastomers 10N, 15N, 20N (see Fig. 5). In general, furthermore, the FE results are seen to be in better agreement with the experimental results for the specimens made with the softer PDMS elastomers. The discussion of all of these observations is deferred to Section 7.

5.2. Homogenization via a theoretical explicit result

By leveraging recent advances in iterative and comparison medium nonlinear homogenization methods (Lopez-Pamies, 2010b; Lopez-Pamies et al., 2013a, b) derived an analytical homogenization result for a general class of filled elastomers for the basic case of interest in this work — namely, for the case when the filled elastomers are free of interphases and can be regarded plainly as two-phase composite materials — that is fully explicit and remarkably simple. Precisely, their result states that the macroscopic nonlinear elastic response of an isotropic incompressible elastomer, whose nonlinear elastic behavior is characterized by any suitably well-behaved stored-energy function of the form $W(\mathbf{F}) = \psi(I_1)$, that is filled with an isotropic distribution of firmly bonded equiaxed — but of arbitrary shape otherwise — rigid particles at volume fraction

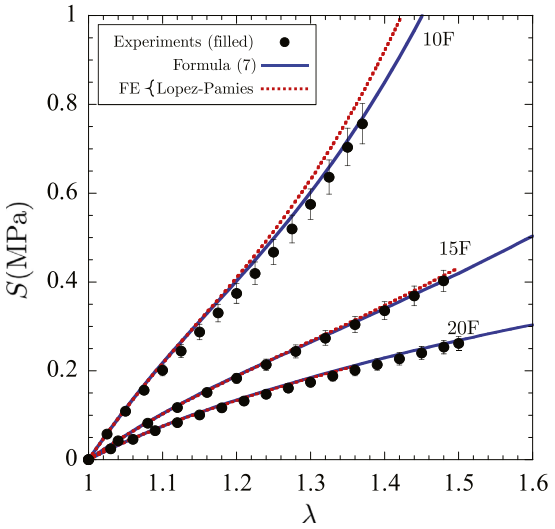

Fig. 9. Comparisons of the homogenization predictions (solid lines) generated from the formula (8) with the experimental data (solid circles) for the uniaxial stress-stretch response of the filled PDMS elastomers 10F, 15F, and 20F. The theoretical results correspond to the case when the underlying PDMS elastomers are modeled with the Lopez-Pamies stored-energy function $(1)_3$ and the material constants given in Table 2. The corresponding FE results (dotted lines) are also included in the figure for further comparison.

c is characterized by the stored-energy function

$$W(\mathbf{F},c)=(1-c)\psi(\mathcal{I}_1)\quad\text{with}\quad\mathcal{I}_1=\frac{I_1-3}{(1-c)^{7/2}}+3 \tag{3}$$

subject to the incompressibility constraint $\det\mathbf{F}=1$.

The interested reader is referred to Sections 3 and 4 in Lopez-Pamies et al. (2013b) for the derivation of the result (3) and for a thorough discussion of its theoretical and practical features. For subsequent use, we spell out two of the latter:

i. *Linearization*. In the limit of small deformations as $\mathbf{F}\to\mathbf{I}$, the stored-energy function (3) reduces asymptotically to

$$W(\mathbf{F},c)=\frac{E_N}{3(1-c)^{5/2}}\operatorname{tr}\varepsilon^2+O\big(||\varepsilon^3||\big) \tag{4}$$

subject to the incompressibility constraint $\operatorname{tr}\varepsilon=\mathbf{0}$. Here, $\varepsilon=(\mathbf{F}+\mathbf{F}^T-2\mathbf{I})/2$ stands for the infinitesimal strain tensor and use has been made of the connection[7] $E_N=6\psi'(3)$, where, again, E_N denotes the initial Young's modulus of the underlying elastomer. It immediately follows from (4) that the stored-energy function (3) implies the result

$$E_F=\frac{E_N}{(1-c)^{5/2}} \tag{5}$$

for the initial Young's modulus of the filled elastomer. Here, it is fitting to remark that expression (5) agrees identically with the classical Brinkman-Roscoe result (*c.f.* Eq. (12) in Roscoe, 1973) for the Young's modulus of an isotropic incompressible linearly elastic solid reinforced by an isotropic distribution of rigid spherical particles of infinitely many diverse sizes. In the dilute limit of small volume fraction of particles as $c\searrow 0$, the Young's modulus (5) reduces asymptotically to the classical Einstein-Smallwood result (*c.f.* Eq. (12) in Smallwood, 1944)

$$E_F=E_N+\frac{5}{2}E_N c+O(c^2). \tag{6}$$

For the case of interest here with $c=0.1$, the formula (5) predicts $E_F=1.30E_N$, while its dilute approximation (6) predicts $E_F=1.25E_N$.

ii. *Specialization to uniaxial stress-stretch loading*. For the case of uniaxial tension, say when $\mathbf{S}=S\mathbf{e}_3\otimes\mathbf{e}_3$ and $\mathbf{F}=\lambda^{-1/2}(\mathbf{e}_1\otimes\mathbf{e}_1+\mathbf{e}_2\otimes\mathbf{e}_2)+\lambda\mathbf{e}_3\otimes\mathbf{e}_3$, the nominal stress-stretch relation implied by the stored-energy function (3) is given by

$$S=(1-c)\frac{\mathrm{d}\psi}{\mathrm{d}\lambda}(\mathcal{I}_1)=\frac{2(\lambda-\lambda^{-2})}{(1-c)^{5/2}}\psi'\left(\frac{\lambda^2+2\lambda^{-1}-3}{(1-c)^{7/2}}+3\right). \tag{7}$$

[7] Throughout this section, we make use of the standard convention $y'=\mathrm{d}y(x)/\mathrm{d}x$ to denote the derivative of functions of a single scalar variable.

When the underlying elastomer is characterized by the Lopez-Pamies model $(1)_3$, i.e., choosing $\psi = \psi_{LP}$, the uniaxial stress-stretch relation (7) specializes to

$$S = (1-c)\frac{\mathrm{d}\psi_{LP}}{\mathrm{d}\lambda}(\mathcal{I}_1) = \frac{\lambda - \lambda^{-2}}{(1-c)^{5/2}}\sum_{r=1}^{2} 3^{1-\alpha_r}\mu_r\left[\frac{\lambda^2 + 2\lambda^{-1} - 3}{(1-c)^{7/2}} + 3\right]^{\alpha_r - 1}. \tag{8}$$

Fig. 9 shows the macroscopic uniaxial stress-stretch response of the filled PDMS elastomers 10F, 15F, and 20F, as predicted by the theoretical homogenization result (8) with the material constants μ_1, μ_2, α_1, α_2 given in Table 2 for the three types of underlying PDMS elastomers with base-to-curing-agent ratios 10:1, 15:1, 20:1 and with volume fraction of particles $c = 10\%$. The experimental results, as well as the corresponding FE results, are included in the figure for direct comparison.

It is immediate that the theoretical results are in good qualitative and quantitative agreement with the three sets of experimental data over the entire range of applied stretches. Together with the FE results presented in Fig. 8, this consistent agreement between the homogenization results and the experiments strongly suggests that the enhancement exhibited by the filled PDMS elastomers 10F, 15F, 20F is by and large solely due to the hydrodynamic effect.

Three other observations are also of note from Fig. 9. The initial Young's modulus E_F predicted by the theory, given by the formula (5), coincides identically with the corresponding FE results reported in Table 3, namely, $E_F = 2.42$, 1.15, and 0.85 MPa for the specimens 10F, 15F, and 20F, respectively. These are within 5% of the experimental values. For finite deformations, the theoretical predictions exhibit a marginally but systematic stiffer stress-stretch response than the experimental data, more so for the specimen 10F. For that same specimen, the theoretical prediction shows a noticeably softer response than the corresponding FE result. These observations are discussed in Section 7.

6. Tension tests of specimens with a cylindrical hole

In this section, we report further evidence indicating that the enhanced elasticity of the filled PDMS elastomers 10F, 15F, 20F is the lone manifestation of the hydrodynamic effect. Complementary to the macroscopically homogeneous deformations of interest in the preceding uniaxial tensions tests, the focus here is on *non-homogeneous* deformations.

For definiteness, we consider the structural response of rectangular specimens that contain a cylindrical hole located at their center. The specimens are clamped at opposite ends and are subjected to a tensile force P that is applied quasistatically. Fig. 10(a) shows a photograph of one such specimen for the case of a filled PDMS elastomer 15F in its undeformed configuration with the various relevant dimensions indicated. Fig. 10(b) shows the same specimen in the deformed configuration at the applied force $P = 20.2$ N, which corresponds in this case to a displacement between the grips of $u = 25.2$ mm.

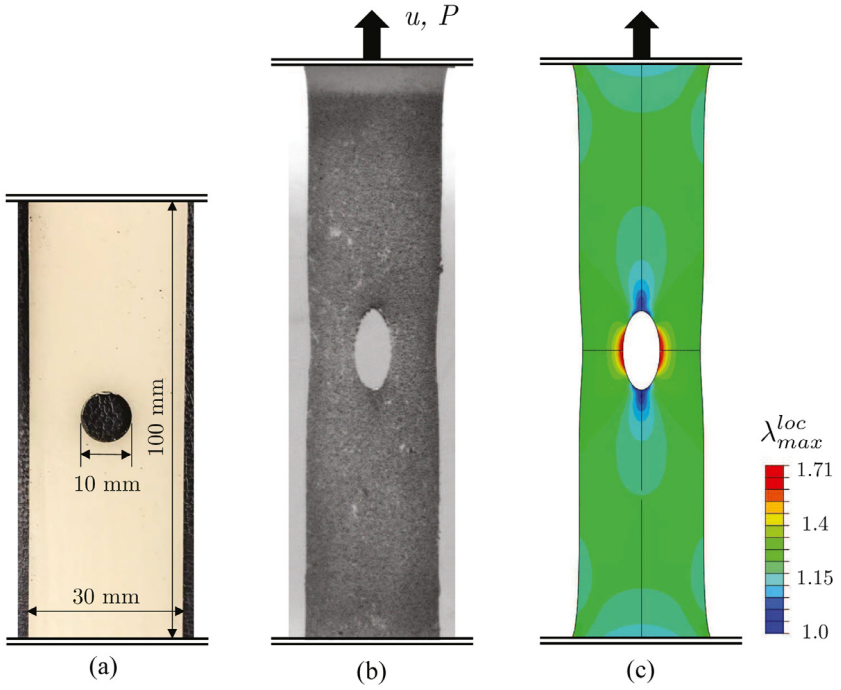

Fig. 10. Photographs and initial dimensions (initial thickness 3 mm) of a 15F specimen with a cylindrical hole in: (a) the undeformed configuration (without speckles) and (b) the deformed configuration (with speckles) at the applied force $P = 20.2$ N corresponding to the displacement $u = 25.2$ mm between the grips. Part (c) shows the FE simulation of the deformed state in (b); the contours correspond to the maximum local stretch.

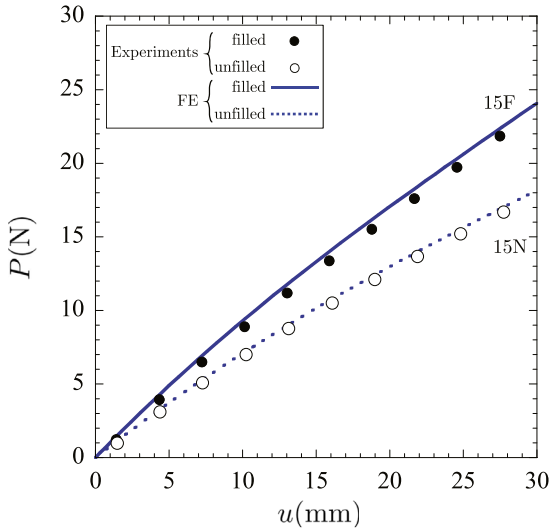

Fig. 11. Comparisons of the total force-displacement response measured experimentally (solid and empty circles) and simulated by FE (solid and dotted lines) for 15F and 15N specimens with a cylindrical hole.

Specimens made with both filled and unfilled PDMS elastomers were fabricated for all three ratios of base to curing agent 10:1, 15:1, 20:1. The fabrication process followed exactly the same steps outlined in Section 2 for the uniaxial tension specimens, with the sole exception that the mold in which they were cured was different. The tests were performed in the same MTS C43 testing system equipped with the same 100 N load cell as the uniaxial tension tests. The displacement u between the grips was measured directly from the testing frame. In addition, DIC was utilized to measure the full displacement field over the surfaces of the deformed specimens.

Figs. 11 shows the total force-displacement response of two specimens, one made with the filled elastomer 15F and the other one made with the corresponding unfilled elastomer 15N. The solid and empty circles stand for the experimental data, whereas the solid and dotted lines stand for the associated theoretical predictions. For the unfilled specimen, the latter correspond to FE simulations wherein the nonlinear elastic behavior of the material is characterized by the Lopez-Pamies model $(1)_3$ with the material constants given in Table 2. For the filled specimen, on the other hand, the theoretical predictions correspond to FE simulations wherein the nonlinear elastic behavior of the material is characterized by the homogenized stored-energy function (3) with $(1)_3$ and the material constants given in Table 2 for the stored-energy function ψ describing the underlying elastomer and, of course, with $c = 10\%$ for the volume fraction of filler particles. As expected from the preceding comparisons, the addition of the glass particles to the PDMS elastomer 15N leads to a significantly stiffer response of the structure, which is again well described by the theoretical predictions solely based on the hydrodynamic effect. The same was true for the 10F and 20F specimens (not reported here).

Fig. 12 shows the contour plots of the displacement components u_2 and u_3 over the surfaces of the 15F specimen at the applied force $P = 20.2$ N, as measured by DIC and as predicted theoretically. Much like with the global force-displacement data reported in Fig. 11, the theoretical predictions are seen to be in qualitative and quantitative agreement with the experimental data.

Because of the large deformations involved, we remark once more that the DIC system did not produce sufficiently accurate strain fields for the specimens with the hole. Accordingly, we do not include those experimental results here. For completeness, however, we do include in part (c) of Fig. 10 the contour plot of the maximum local stretch $\lambda_{\max}^{loc}$ predicted theoretically over the surface of the 15F specimen at the applied force of $P = 20.2$ N. The heterogeneity of $\lambda_{\max}^{loc}$ is obvious there. It is also worth remarking that the maximum local stretch attains its largest value $\lambda_{\max}^{loc} = 1.71$ at the longitudinal poles of the hole.

7. Discussion and conclusions

The close qualitative and quantitative agreement between the computational and analytical homogenization results with the experiments shown in Figs. 8, 9, 11, and 12 involving homogeneous and non-homogeneous macroscopic deformations point to the fact that the observed enhancement in the nonlinear elastic response of all the three PDMS elastomers 10N, 15N, 20N upon the addition of the glass particles is indeed solely due to the hydrodynamic effect. To our knowledge, this is the first set of experimental/theoretical results in the literature that has isolated and quantified this omnipresent effect in filled elastomers under finite deformations.

The analysis of the experimental results has also revealed a number of important practical issues. For instance, regarding the experimental measurements themselves, a maximum variation of about 6% in the uniaxial stress-stretch response was

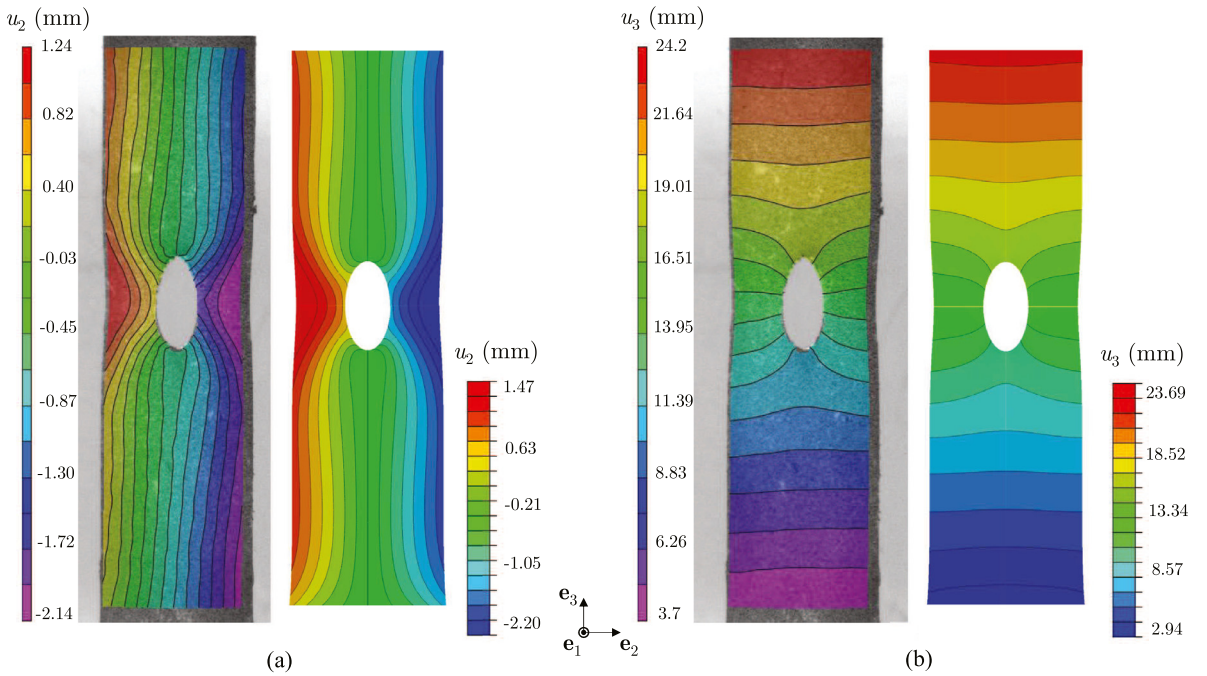

Fig. 12. Comparisons of the full displacement fields u_2 and u_3 measured by DIC and simulated by FE for a 15F specimen with a cylindrical hole. The results correspond to the applied force $P = 20.2$ N and are shown in the deformed configuration. Part (a) shows the comparison for the displacement component u_2 transverse to the applied force, while part (b) shows the comparison for the displacement component u_3 in the direction of the applied force.

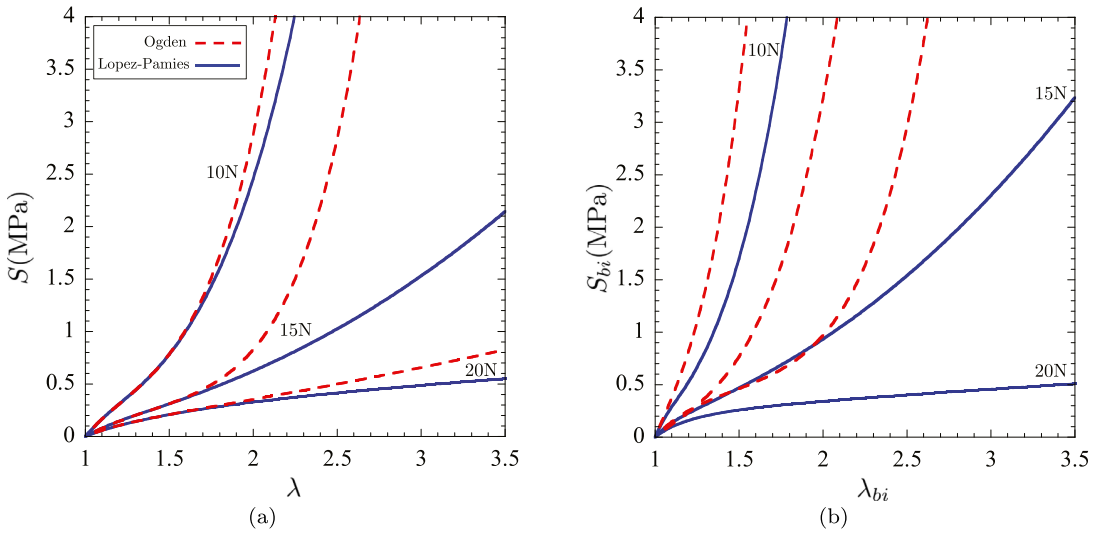

Fig. 13. (a) Uniaxial and (b) biaxial stress-stretch responses of the unfilled PDMS elastomers 10N, 15N, and 20N. The results correspond to the Ogden $(1)_2$ and the Lopez-Pamies $(1)_3$ hyperelastic models with the material constants listed in Table 2.

observed among specimens of the same type. This appeared to be mostly due to the fact that the underlying elastomers of a given type may not have had exactly the same ratio of base to curing agent and therefore exhibited slightly different cross-link densities. Further plausible sources behind the observed differences could also be attributed to the facts that the amounts of filler particles were not exactly the same and/or that there was a different degree of debonding of some of the particles during the loading, from specimen to specimen.

That there was some but minor particle debonding in the experiments is consistent with the stiffer responses persistently exhibited by the theoretical predictions, especially for the filled elastomers made with the stiffest PDMS elastomer, that is,

again, the one with the ratio 10:1 of base to curing agent, which has been reported[8] to exhibit a relatively weaker adhesion to glass than those with ratios 15:1 and 20:1. Howbeit, a combination of simulations accounting for debonding and DIC analyses on the change in volume of the deformed specimens (not reported here) has indicated that if there was debonding in the experiments, this must have been necessarily small.

Regarding the slight quantitative differences between the experiments and the theoretical predictions, it is also important to emphasize that the latter were generated based on hyperelastic descriptions of the underlying PDMS elastomers 10N, 15N, 20N whose parameters were fitted to uniaxial stress-stretch data. Now, the maximum macroscopic stretch achieved during the uniaxial tests did not exceed $\lambda_{max} = 1.6$ because the specimens failed due to fracture near the grips. However, as illustrated by Fig. 7, the local stretches within the elastomers in the filled specimens were multi-axial and reached values larger than $\lambda^{loc} = 3$ far exceeding the applied maximum macroscopic stretch $\lambda_{max} = 1.6$. This entails that the material constants listed in Table 2 that were utilized in the models (1) for the PDMS elastomers 10N, 15N, 20N may not necessarily be the most adequate. To further illustrate the significance of this point, Figs. 13(a) and (b) show the uniaxial and biaxial stress-stretch responses for the three unfilled PDMS elastomers 10N, 15N, 20N, as characterized by the Ogden $(1)_2$ and the Lopez-Pamies $(1)_3$ models with the material constants listed in Table 2. While both models exhibit essentially identical behaviors up to about $\lambda = 1.7$ in uniaxial tension, as already established by Fig. 5, they are drastically different for larger uniaxial stretches. The differences are even more severe for biaxial loading. These point to the potential limitations of fitting hyperelastic models only to a uniaxial data; see, e.g., Ogden et al. (2004).

Finally, we note that the fundamental results presented in this work have direct practical implications on the modeling of emerging soft active materials, such as for instance magnetorheological elastomers. Indeed, as opposed to conventional filled elastomers wherein the filler particles are nanometer in size, the iron filler particles in magnetorheological elastomers are typically micrometer in size; see, e.g., Diguet et al. (2010), Danas et al. (2012) and Lefèvre et al. (2017). Accordingly, their macroscopic mechanical response is likely to be described in terms solely of the mechanical response of their underlying elastomeric matrix and the hydrodynamic effect provided by the iron filler particles.

Acknowledgments

This work was supported in part by the National Science Foundation through the Grant CMMI-1661853.

Supplementary material

Supplementary material associated with this article can be found, in the online version, at doi:10.1016/j.jmps.2019.103781.

References

ABAQUS Version 6.14 Documentation, 2014. Dassault Systemes Simulia Corp.Providence, RI, USA.
Benevides, R.O., Nunes, L.C.S., 2015. Mechanical behavior of the alumina-filled silicone rubber under pure shear at finite strain. Mech. Mater. 85, 57–65.
Bergström, J.S., Boyce, M.C., 1999. Mechanical behavior of particle-filled elastomers. Rubber Chem. Technol. 69, 781–785.
Berriot, J., Martin, F., Montes, H., Monnerie, L., Sotta, P., 2003. Reinforcement of model filled elastomers: characterization of the crosslinking density at the filler-elastomer interface by 1h NMR measurements. Polymer 44, 1437–1447.
Braides, A., 1985. Homogenization of some almost periodic coercive functionals. Rend. Accad. Naz. XL 9, 313–322.
Chi, H., Lopez-Pamies, O., Paulino, G.H., 2016. A variational formulation with rigid-body constraints for finite elasticity: theory, finite element implementation, and applications. Comput. Mech. 57, 325–338.
Danas, K., Kankanala, S.V., Triantafyllidis, N., 2012. Experiments and modeling of iron-particle-filled magnetorheological elastomers. J. Mech. Phys. Solids 60, 120–138.
Diguet, G., Beaugnon, E., Cavaillé, J.Y., 2010. Shape effect in the magnetostriction of ferromagnetic composite. J. Magn. Magn. Mater. 322, 3337–3341.
Einstein, A., 1906. Eine neue bestimmung der moleküldimensionen [A new determination of molecular dimensions]. Ann. Phys. 324, 289–306.
Frogley, D., Ravich, D., Wagner, H.D., 2003. Mechanical properties of carbon nanoparticlereinforced elastomers. Compos. Sci. Technol. 63, 1647–1654.
Fukahori, Y., 2007. Generalized concept of the reinforcement of elastomers. part 1: carbon black reinforcement of rubbers. Rubber Chem. Technol. 80, 701–725.
Goudarzi, T., Spring, D.W., Paulino, G.H., Lopez-Pamies, O., 2015. Filled elastomers: A theory of filler reinforcement based on hydrodynamic and interphasial effects. J. Mech. Phys. Solids 80, 37–67.
Govindjee, S., Simo, J., 1991. A micromechanically based continuum damage model for carbon black-filled rubbers incorporating mullins effect. J. Mech. Phys. Solids 39, 87–112.
Gusev, A.A., 1997. Representative volume element size for elastic composites: a numerical study. J. Mech. Phys. Solids 45, 1449–1459.
Guth, E., Gold, O., 1938. On the hydrodynamical theory of the viscosity of suspensions. Phys. Rev. 53, 322.
Heinrich, G., Klüppel, M., Vilgis, T.A., 2002. Reinforcement of elastomers. Curr. Opin. Solid State Mater. Sci. 6, 195–203.
Hill, R., 1972. On constitutive macro-variables for heterogeneous solids at finite strain. Proc. R. Soc. Lond. A 326, 131–147.
Johnston, I.D., McCluskey, D.K., Tan, C.K.L., Tracey, M.C., 2014. Mechanical characterization of bulk sylgard 184 for microfluidics and microengineering. J. Micromech. Microeng. 24, 035017.
Leblanc, J.L., 2010. Filled Polymers: Science and Industrial Applications. CRC Press, Boca Raton.

[8] The work of Poulain et al. (2017) provides a lower bound of about 2.5 MPa in the value of the Cauchy hydrostatic stress at the interfaces between the PDMS and the glass beads below which debonding does not occur for filled PDMS elastomers 15F and 20F. For the filled PDMS elastomer 10F, debonding may or may not occur at Cauchy hydrostatic stresses of about 2.5 MPa or larger. According to the FE simulations outlined in Section 5.1, the maximum value of the local Cauchy hydrostatic stress σ_h remains mostly below 2.5 MPa for all three types of filled PDMS elastomers 10F, 15F, and 20F; see, e.g., Fig. 7. Thus, no significant degree of debonding is expected to occur.

Lefèvre, V., Danas, K., Lopez-Pamies, O., 2017. A general result for the magnetoelastic response of isotropic suspensions of iron and ferrofluid particles in rubber, with applications to spherical and cylindrical specimens. J. Mech. Phys. Solids 107, 343–364.
Lefévre, V., Lopez-Pamies, O., 2017a. Nonlinear electroelastic deformations of dielectric elastomer composites: I — ideal elastic dielectrics. J. Mech. Phys. Solids 99, 409–437.
Lefévre, V., Lopez-Pamies, O., 2017b. Nonlinear electroelastic deformations of dielectric elastomer composites: II — non-gaussian elastic dielectrics. J. Mech. Phys. Solids 99, 438–470.
Lopez-Pamies, O., 2010a. A new I_1-based model for rubber elastic materials. Comptes Rendus Mécanique 338, 3–11.
Lopez-Pamies, O., 2010b. An exact result for the macroscopic response of particle-reinforced neohookean solids. J. Appl. Mech. 77, 021016.
Lopez-Pamies, O., Goudarzi, T., Nakamura, T., 2013a. The nonlinear elastic response of suspensions of rigid inclusions in rubber: I — An exact result for dilute suspensions. J. Mech. Phys. Solids 61, 1–18.
Lopez-Pamies, O., Goudarzi, T., Danas, K., 2013b. The nonlinear elastic response of suspensions of rigid inclusions in rubber: II — A simple explicit approximation for finite concentration suspensions. J. Mech. Phys. Solids 61, 19–37.
Lopez-Pamies, O., Ponte Castañeda, P., 2006. On the overall behavior, microstructure evolution, and macroscopic stability in reinforced rubbers at large deformations: I — Theory. J. Mech. Phys. Solids 54, 807–830.
Mark, J.E., Erman, B., 2007. Rubberlike Elasticity: A Molecular Primer. Cambridge University Press.
Meddeb, A.B., Tighe, T., Ounaies, Z., Lopez-Pamies, O., 2019. Extreme enhancement of the nonlinear elastic response of elastomer nanoparticulate composites via interphases. Compos. Part B 156, 166–173.
Meinecke, E.A., Taftaf, M.I., 1988. Effect of carbon-black on the mechanical properties of elastomers. Rubber Chem. Technol. 61, 534–547.
Michel, J.C., Moulinec, H., Suquet, P., 1999. Effective properties of composite materials with periodic microstructure: a computational approach. Comput. Methods Appl. Mech. Eng. 172, 109–143.
Mooney, M., 1940. A theory of large elastic deformation. J. Appl. Phys. 11, 582–592.
Müller, S., 1987. Homogenization of nonconvex integral functionals and cellular elastic materials. Arch. Rat. Mech. Anal. 99, 189–212.
Mullins, L., Tobin, N.R., 1965. Stress softening in rubber vulcanizates. Part I. use of a strain amplification factor to describe the elastic behavior of filler-reinforced vulcanized rubber. J. Appl. Polym. Sci. 9, 2993–3009.
Ogden, R.W., 1972. Large deformation isotropic elasticity — on the correlation of theory and experiment for incompressible rubberlike solids. Proc. R. Soc. Lond. A 326, 565–584.
Ogden, R.W., Saccomandi, G., Sgura, I., 2004. Fitting hyperelastic models to experimental data. Comput. Mech. 34, 484–502.
Poulain, X., Lefèvre, V., Lopez-Pamies, O., Ravi-Chandar, K., 2017. Damage in elastomers: nucleation and growth of cavities, micro-cracks, and macro-cracks. Int. J. Fract. 205, 1–21.
Poulain, X., Lopez-Pamies, O., Ravi-Chandar, K., 2018. Damage in elastomers: healing of internally nucleated cavities and micro-cracks. Soft Matter 14, 4633–4640.
Qu, M., Deng, F., Kalkhoran, S.M., Gouldstone, A., Robisson, A., Van Vliet, K.J., 2011. Nanoscale visualization and multiscale mechanical implications of bound rubber interphases in rubber carbon black nanocomposites. Soft Matter 7, 1066–1077.
Roscoe, R., 1973. Isotropic composites with elastic or viscoelastic phases: general bounds for the moduli and solutions for special geometries. Rheol. Acta 12, 404–411.
Schöbel, J., 1997. Netgen an advancing front 2d/3d-mesh generator based on abstract rules. Comput. Visual. Sci. 1, 41–52.
Segurado, J., Llorca, J., 2002. A numerical approximation to the elastic properties of sphere-reinforced composites. J. Mech. Phys. Solids 50, 2107–2121.
Smallwood, H.M., 1944. Limiting law of the reinforcement of rubber. J. Appl. Phys. 15, 758–766.
Song, Y., Zheng, Q., 2016. Concepts and conflicts in nanoparticles reinforcement to polymers beyond hydrodynamics. Prog. Mater. Sci. 84, 1–58.
Spinelli, S.A., Lefèvre, V., Lopez-Pamies, O., 2015. Dielectric elastomer composites: a general closed-form solution in the small-deformation limit. J. Mech. Phys. Solids 83, 263–284.
Tadiello, L., D'Arienzo, M., Di Credico, B., Hanel, T., Matejka, L., Mauri, M., Morazzoni, F., Simonutti, R., Spirkovac, M., Scotti, R., 2015. The filler-rubber interface in styrene butadiene nanocomposites with anisotropic silica particles: morphology and dynamic properties. Soft Matter 11, 4022–4033.
Valentin, J.L., Mora-Barrantes, I., Carretero-Gonzalez, J., Lopez-Manchado, M.A., Sotta, P., Long, D.R., Saalwächter, K., 2008. Uncertainties in the determination of cross-link density by equilibrium swelling experiments in natural rubber. Macromolecules 41. 4717–4129
Wagner, M.P., 1976. Reinforcing silicas and silicates. Rubb. Chem. Technol. 49, 703–774.
Wiegand, W.B., 1937. The carbon reinforcement of rubber. Rubb. Chem. Tech. 10, 395–411.
Zou, H., Wu, S., Shen, J., 2008. Polymer/silica nanocomposites: preparation, characterization, properties, and applications. Chem. Rev. 108, 3893–3957.